ORNL/TM-11971
(CESAR-91/39)

ornl

OAK RIDGE
NATIONAL
LABORATORY

MARTIN MARIETTA

Phase I Report on Sensor Technology, Data Fusion and Data Interpretation for Site Characterization

Martin Beckerman

MANAGED BY
MARTIN MARIETTA ENERGY SYSTEMS, INC.
FOR THE UNITED STATES
DEPARTMENT OF ENERGY

ORNL/TM-11971
CESAR-91/39

Engineering Physics and Mathematics Division

PHASE I REPORT ON SENSOR TECHNOLOGY, DATA FUSION AND DATA INTERPRETATION FOR SITE CHARACTERIZATION

Martin Beckerman

DATE PUBLISHED - October 1991

Research sponsored by the
Office of Technology Development,
U.S. Department of Energy

Prepared by the
OAK RIDGE NATIONAL LABORATORY
Oak Ridge, Tennessee 37831
Managed By
MARTIN MARIETTA ENERGY SYSTEMS, INC.
for the
U.S. DEPARTMENT OF ENERGY
under Contract No. DE-AC05-84OR21400

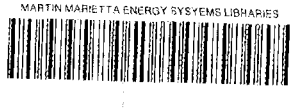

CONTENTS

LIST OF FIGURES

Figure No.

List of Figures (Cont'd)

Figure No.

ABSTRACT

In this report we discuss sensor technology, data fusion and data interpretation approaches of possible maximal usefulness for subsurface imaging and characterization of land-fill waste sites. Two sensor technologies, terrain conductivity using electromagnetic induction and ground penetrating radar, are described and the literature on the subject is reviewed. We identify the maximum entropy stochastic method as one providing a rigorously justifiable framework for fusing the sensor data, briefly summarize work done by us in this area, and examine some of the outstanding issues with regard to data fusion and interpretation.

1. INTRODUCTION

The non-evasive detection and characterization of trenches, pipes, drums, and other metallic and dielectric materials of varying numbers, sizes and orientations buried at shallow depths below the surface is an important task within the DOE Environmental Restoration and Waste Management program. In this draft report we discuss two sensor technologies - electromagnetic induction, specifically the EM31 terrain conductivity meter, and ground penetrating radar - in the context of the characterization of land-fill waste sites.

The central problem in characterizing a subsurface site is that the inversion process, that is, the process of transforming a set of subsurface image data into a representation of the environment, is not unique. This "inverse problem" is encountered in diverse areas of study such as radioastronomy, tomography, robotics and geophysics. The problem arises whenever there is noisy and missing data, or insufficient data to disambiguate among differing interpretations (systematic errors), or incompletely known detector parameters and responses.

The term "data fusion", or equivalently "multi-sensor data fusion", denotes the task of combining data and information from more than one sensor location, and/or more than one sensor or other data source, in order to generate a reliable and consistent representation of the environment. Within the data fusion framework, maximum entropy methods provide a unique and self-consistent means for generating representations.

This report is organized, as follows. The terrain conductivity meter and ground penetrating radar systems, the imaging data acquired, and environmental factors affecting their performance are described in Section 2. The maximum entropy method is outlined in Section 3. Examples of this method from geophysics, and from other areas where inversion problems are encountered, are presented together with a brief summary of our work in this area. Results from field studies and modelling investigations reported in the literature are summarized in Section 4. The focus in this summary is on those aspects and issues which pertain to data interpretation. We conclude the report in Section 5.

2. SENSOR TECHNOLOGY

2.1 TERRAIN CONDUCTIVITY

The EM31 terrain conductivity sensor, manufactured by Geonics, Ltd., employs a transmitting coil and a receiving coil separated from one another by a fixed distance on a boom of 3.66 m, and operating at a fixed frequency of 9.8 Khz. The transmitting coil functions as a magnetic dipole, inducing eddy currents in the ground. These eddy currents, in turn, induce a secondary magnetic field, shifted in phase from the primary field. The receiving coil also functions as a dipole, and senses the primary field and the components of the secondary field 90 degrees out of phase with the primary field (the quadrature component)) and also the component in phase with the primary field (the in-phase component).

In many applications the ratio of the quadrature field to the primary field is directly proportional to the terrain conductivity. More specifically, we have the relation

$$\sigma = \frac{4}{2\pi f \mu_0 S^2}\left(\frac{H_s}{H_p}\right)$$

where f is the frequency, μ_0 is the permeability of free space, s is the coil separation, H_p is the primary magnetic field at the receiver coil, H_s is the secondary magnetic field at the receiver coil, and σ is the ground conductivity [16].

The in-phase component does not have as simple a physical interpretation, but this component of the field is more sensitive than the quadrature component to buried metallic objects. As noted by Nyquist and Blair [19], in hazardous waste sites where there is a variety of types of buried metallic objects such as drums and pipes, the simple linear relationship between quadrature to primary ratio and conductivity breaks down. The main signature then becomes large departures from background. That is, contrasts in readings from adjacent locations provide the main source of information on buried objects. The EM31 was used to survey the SWSA 4 site at ORNL by Nyquist and Blair [19]. They found that the quadrature and in-phase data showed similar trends, but the authors did find that the in-phase data was superior for delineating trench boundaries. Results of their work are shown in Figs. 1-3.

The EM31 can be operated with the coils horizontal or with the coils vertical with respect to the ground. The response of the coils to materials at various depths is different in the two cases. As displayed in Fig. 4 we see that in the

horizontal configuration the coils are most sensitive to materials buried near the surface, and the response falls off monotonically with depth. In the vertical configuration, the coils are not sensitive to surface material, but rather have a peak sensitivity at depths on the order of 0.5 z, where z is the depth to coils spacing ratio.

Both configurations were used by Frohlich and Lancaster [9] in their archaeological applications. The effective penetration is 6 m in the vertical configuration, and 3 m in the horizontal mode. The authors successfully used this sensor in arid and semi-arid Middle-Eastern environments. The authors noted some deterioration in performance in the few cases where data were collected after it had rained.

2.2 GROUND PENETRATING RADAR

Depicted in Fig. 5 is a block diagram of a typical ground penetrating radar system used for subsurface characterization. These systems contain a radar module usually shock mounted in a vehicle, and a unit which is towed along the transect lines. The towed unit may have a single transmitter/receiver antenna or have separate transmitting and receiving antennas. Typically there is a graphic recording device for displaying the received and processed signals and/or there is a tape recorder for later playback.

A number of antennas, each one emitting a broad spectrum of frequencies are usually provided. In the study by Horton et al [13] the central frequencies were 10, 80, 120 and 300 Mhz; in the investigation by Collins, et al [5] the central frequencies were 80, 120, 300, 400 and 500 Mhz. The frequency spectra of the antennas used by Horton are shown in Fig. 6. In general, low frequency antennas are capable of probing to greater depths than high frequency units. High frequency (on the order of 1 GHz) antennas give greater resolution data and are most useful for locating objects buried near the surface.

The ground penetrating radar units transmit pulses of short duration into the ground. For the system used by Horton the pulse rise time was 1 nanosecond (nsec), the pulse width was 3 nsec, and the pulse repetition rate was 51.2 Khz. As shown in Fig. 5, when an electromagnetic pulse strikes an interface between two media having different dielectric constants, part of the energy is reflected back to the surface. This reflected signal is then detected and processed.

As subsurface media become progressively more conductive, the rate of attenuation of the electromagnetic energy increases. Therefore, besides the dependence upon the characteristics of

the radar unit, the maximum depth of penetration which can be achieved depends upon the conductivity of the media, the differences between the dielectric constants of the media, and the distances to the interfaces. The conductivity of the media, in turn, depends upon the moisture content, the proportion and types of clays, and the amount and types of salts in solution. The maximum depths possible vary from 0.5 m to 25 m, depending upon the aforementioned quantities. Conductivity, and the dielectric constant, will be discussed further in Section 2.3.

Shown in Fig. 7 is a schematic diagram of the typical received waveform and a corresponding display of the output by a grey-scale graphic recorder. In this figure we observe dark bands corresponding to signal peaks, separated by narrow white bands denoting zero crossings. In processing the signals a time-domain progressive sampling of the repetitive pulses is used to produce a waveform having a shape similar to the nanosecond pulses, but with a millisecond time base for use by the graphic recorder.

2.3 SUBSURFACE ENVIRONMENTAL FACTORS

2.3.1 Conductivity of Soils

Soils are classified according to grain size into sand, silt and clay. Grain size diameters for sand range from 0.05 to 2.0 mm, and those for silt vary from 0.002 to 0.05 mm. Clay grain size diameters are less than 0.002 mm. Clay grain size can be further divided into coarse-grained (0.001-0.002 mm in diameter) and fine-grained (< 0.001 mm). The latter group is composed of micro-crystalline particles, exhibiting a sheet-like (layered) structure. Exchangeable ions are commonly held between the sheets of the crystal lattice include Ca, Na, K, H and Mg ions. These ions greatly increase the electrical conductivity of the material.

The conductivity of soils is strongly dependent upon the clay content and clay type, the moisture content and the moisture salinity. Listed in Table 1 are cation electrical conductivities (CEC) for three representative types of clay. Units are millequivalents (me) per 100 grams. Montmorillonite has a high CEC while kaolinite has a CEC comparable to that for sand. A high clay content may or may not limit the penetration depths possible. If the CEC of the clay is not high, and the clay is dry the radar signals will still penetrate and provide good resolution. Typical GPR penetration depths range from 5 to 25 m in coarse-grained soils, from 2 to 5 m in moderately coarse-grained soils, to from less than 0.5 m to 1.5 m in fine-grained soils [5].

2.3.2 Conductivity of Rock

In most rocky material the porosity and chemical content of the water-filled porous spaces governs the resistivity more than the mineral grains in the rock itself. The salinity of the water in the pores is the most crucial factor determining resistivity. In sedimentary rock the porosity is primarily inter-granular, and consists of voids remaining after compactification. In igneous and metamorphic rock the inter-granular pores are quite small. The main conduit for moisture is through cracks and fractures. Thus, in the absence of substantial fracturing (joints) igneous and metamorphic rock will have low conductivity. The conductivities of sedimentary rock varies from low for dense sandstone and limestone to moderate for porous sandstones and limestones, and shale.

2.3.3 Dielectric Constant

There have been several investigations of the relationship between soil-solution porosity and dielectric constant. In the recent work by Arulanandan [1] it was shown that knowledge of the dielectric constant of the saturated soils in the horizontal and vertical directions at high frequencies of around 50 Mhz provides the necessary data for evaluation of the porosity of most soils when the dielectric constants of the particles and solution are known. The frequency dependence of the dielectric constant [1] is shown in Fig. 8 for a variety of soils. In situ applications as well as the laboratory uses of this relationship was noted by the author.

In another, earlier study Wobschall [25] found that in the high frequency (1 MHz to 1 GHz) limit the dielectric constant and conductivity of soil is primarily a function of its water content. In those cases where higher clay dielectric constants are found the general form for the dielectric constant versus volume fraction of water curve is similar.

3. DATA FUSION

3.1 PRINCIPLE OF MAXIMUM ENTROPY

The principle of maximum entropy provides us with a means for determining appropriate forms for the probabilities from experimental data. Let p denote a probability density over a discrete space $V = (v_1, v_2, \ldots, v_n)$. . In discrete form the corresponding Shannon-Jaynes entropy, S, is given by the expression

$$S = \sum_i p(v_i) \ell n p(v_i), \quad i = 1, 2, \ldots, n \quad .$$

The probabilities of interest are those which maximize S subject to the normalization condition

$$\sum_i p(v_i) = 1$$

and the data provided constraint equations

$$\sum_i q_k(v_i)p(v_i) = < q_k > , k = 1, \ldots , m;\ m < n \quad .$$

Using the Lagrange multiplier technique a formal solution to this variational problem can be found, namely,

$$p(v_i) = e^{-\lambda - \sum_k \lambda_k q_k(v_i)}$$

where the constants λ and λ_k are Lagrange multipliers. Similar expression can be written for the continuous case.

A generalized entropy can also be defined. This entropy takes the form

$$S = \sum_i p(v_i)\ell n[p(v_i)/r(v_i)]$$

In expressions of this type the probability density $r(v_i)$ can serve as an initial model of the image [11]. Expressions of this form have been termed the cross entropy between p and r, when p and r represent any two probability densities [22].

3.2 APPLICATIONS TO IMAGE DATA

Maximum entropy reconstruction methods have been used in many fields where difficult inverse problems have been encountered. These methods have been used for image reconstruction in radio astronomy, neutron physics, tomography, robotics and geophysics. As mentioned in the Introduction, the underlying problem is that of the non-uniqueness of the inverse. This type of problem is encountered whenever the data are noisy and incomplete, and when the instrument response function is not completely known. In the inversion process there is a trade-off between resolution and accuracy [20], and one would like the reconstructed images to be free from artifacts.

Applications to geophysics begin with the pioneering papers on

power spectra analysis by Lacoss [15] and by Burg [3]. A more recent application to power spectra was carried out by Shore [22]. His method differed from that of the earlier works of Lacoss and Burg by the explicit inclusion of a prior distribution of the power spectra. This prior is used together with new information in the form of an autocorrelation function. In place of the usual maximum entropy spectral analysis Shore introduces the principle of minimum cross entropy to yield a family of spectral estimators consistent with the known autocorrelations.

In another study Sibisi [23] applied the maximum entropy method to Fourier transform nuclear magnetic resonance data. In this work frequency and decay information were recovered from time-series data. Factors making this an ill-posed problem include possible misalignment of the detector and distortion-corrupted early data points.

In a yet more recent study, Jacobs and van der Geest [14] use maximum entropy methods to invert band-limited seismic traces. These seismic traces represent blurred images of the local reflectivity trace of the earth. The reconstructed traces can be modelled as reflectivity traces convolved with a wavelet and corrupted by noise. The problem addressed is that the enhancement of the images to full bandwidth reflectivity traces from the seismic data is underdetermined, that is, extra information is needed to obtain a unique inverse.

Turning to robotics we find that a maximum entropy method was applied to object identification by Beckerman [2]. In the study ultrasound and visual image data were acquired using a mobile robot. After an initial processing stage the ultrasound data were mapped into the visual sensor domain in order to disambiguate among a large number of candidate edge segments. Bayesian updating was done using a maximum entropy distance measure, determined by constraining the mean distance between ultrasound and visual points of interest in the dual ultrasound-visual representation.

As noted by Gull and Daniell [10], and by Gull and Skilling [11], a maximum entropy image contains just enough structure to fit the data, and no more. These images provide a unique solution to the inverse problem, and constitute the only consistent way to combine different data into a single positive image. Displayed in Fig. 9 are two maximum entropy (MaxEnt) maps from [2] of a laboratory environment containing several objects identified by means of the ultrasound sensor scan. The second map differs from the first map in that additional information has been used to update and correct for distortion errors.

MaxEnt maps have been produced by Gull and Daniell [10] from both radio and x-ray data. X-ray counting rates for various positions near the supernova remnant Cassiopeia A are shown in Fig. 10. Also displayed is a contour map depicting the point spread function, and below that a MaxEnt map of Cassiopeia A. Conventional and MaxEnt reconstructions of radio data for 3C66 are compared to one another in Fig. 11. While we observe negative regions in the conventional reconstruction, all regions of the MaxEnt map are positive and regions of low surface brightness are clearly visible.

4. DATA INTERPRETATION

4.1 FIELD STUDIES USING TERRAIN CONDUCTIVITY

In a recent study by Dalan [6], the EM31 terrain conductivity sensor was used to study and map leveled earthen burial mounds and palisades in the Cahokia Mounds State Historic Site in southwestern Illinois. Results of EM31 transect across a well defined mound are shown in Fig. 12. We observe in these conductivity profiles a low conductivity anomaly, i.e., high conductivity along the edges of the mound, and, lowest conductivity at the crest. In surveying other mounds similar profiles were superimposed on an overall gradient caused by a buried ridge and shale system, except for one mound which appeared as a high conductivity anomaly, due most likely to the presence of clay fill. It was surmised that the differences in mound conductivities were due to variations in fill material.

Conductivity profiles for one of the palisades are displayed in the next figure (Fig. 13). Here we observe a complex set of anomalies for each transect (Fig. 14). As noted by Dalan the horizontal resolution is approximately that of the coil separation. For the EM31 unit the resolution is 3.6 m ; for the EM38 sensor the corresponding value is 1.0 m. In practice the minimum values reported by Dalan are on the order of 1-2 m. Filled trenches typically producing one or two conductivity lows with a magnitude of approximately 3mS/m and widths of 2 m were located. The linearity of the anomaly seen in the profile across transect is an important distinguishing feature.

4.2 FIELD STUDIES WITH GROUND PENETRATING RADAR

In the extensive field study by Horton, et. al [13] data were collected at three low level waste sites (Maxey Flats, KY; Beatty, NV; Sheffield, IL) and one test site (Harvard, MA). In processing and interpreting the data from these sites the

authors performed pre-processing to remove background noise, to smooth the remaining data and remove specular reflection bands. The dominant features remaining were then extracted and their patterns identified. Models were developed in order to understand the defining features for typical subsurface objects.

An enlargement of a pair of processed radar images is displayed in Fig. 15. The left-hand image is of a vertical barrel. This image possesses a specular bump which is absent in the right-hand image which is of a horizontal barrel. More generally, the shapes and numbers of crescents differ for the two orientations. However, there may be some ambiguities in the identification of crescents. The next figure (Fig. 16) shows these crescents after further processing.

In their report Horton, et. al. [13] stressed the need for objective, automated data processing and identification. Such an automated methods for system would include digital filtering (frequency analysis), target recognition and identification techniques. These systems would also treat anomalies, artifacts and detector effects whenever they occur.

In another field study the problem of imaging metallic and plastic pipes buried at shallow depths of up to 2.5 m was studied by a group at Hitachi. The specific problem addressed in the study was the operation of ground penetrating radar in wet soil conditions. As noted by Michiguchi, et al [18] the attenuation rate of radio waves propagating in soil increases from 5 to 20 Db/m as the water content increases. The unit developed by this group operated at a central frequency of 100 MHz with a repetition rate of 1 MHz. They observed that to operate in unfavorable detecting conditions the radar unit should have a dynamic range of over 100 dB. By varying both a time-varying gain and a constant selectable gain the authors were able to achieve a dynamic amplifier range of about 80 dB. The total range, including the power control range, exceeded the 100 dB requirement.

To achieve the desired performance fast image processing methods, a pre-processing stage and synthetic aperture approach were employed. Results after image processing for a steel pipe buried at a depth of 2.5 m under conditions where an averaged attenuation rate was 12.6 dB/m (total attenuation was 63 dB) are displayed in Fig. 17. A plastic pipe buried at a depth of 1 m was also imaged by the system. The pre-processing and synthetic aperture processing methodologies are described in further detail in [17]. The primary function of the pre-processing stage was the removal of clutter noise from the reflected signals. To do so variations in phase difference between the reflected signals and a reference

signal were analyzed to extract the phase profiles. In the synthetic aperture stage of processing, the propagation times extracted from the pre-processing stage were used to construct an image of the buried object.

4.3 MODELLING AND INTERPRETATION OF GPR DATA

The goal in a number of studies reported in the literature was the modelling of the response of ground penetrating radars to various buried objects. In the study by Hill [12] plane wave scattering matrix methods were used to determine the response to buried dielectric scatterers. Numerical results were obtained using the Born approximation to derive the scattering matrix for scattering of small dielectric contrast. In this study the plane-wave transmitting and receiving characteristics of a UHF detector consisting of oppositely directed transmitting dipoles and a dipole receiver were determined. Included in the modelling were effects of the air-surface interface. The calculated sweep curves were found to be symmetric with a null directly over the target. Experimental results were qualitatively similar.

In the investigation by Schneider et al [21] the scattering from subsurface dielectric ellipsoids was modelled using a T-matrix method. In this approach restrictions to two-dimensions were not needed, and the source could have an arbitrary orientation with respect to the scatterer. The theory was tested using a laboratory scale model. In the experiments PVC tubes were used to define the tunnels, and sleeve dipole antenna were used for both transmitting and receiving. The experimental data were obtained in the frequency domain for frequencies in the range 2 to 4 GHz. Two-dimensional and three dimensional predictions were compared with the experimental results for cross-borehole scattering. The authors concluded that the T-matrix results compared favorably with the experimental results while providing the all the diagnostic capabilities of the two-dimensional approach.

In the modelling study by Smith and Scott [24], a red clay earth environment was represented by a mixture of mineral oil, saline solution and a stabilizing agent. A 1/3 full size radar system operating in the frequency range 150 MHz to 1.5 GHz was built. The authors noted that the radar antennas were lousy and dispersive, their characteristics depended upon their location above the earth, and were difficult to model theoretically. The laboratory-size scale model was therefore useful in determining responses for different antennas and target orientations, compositions, etc.

Before closing this section, the work by Das, et. al [7], [8] should be noted. In these papers the authors report results of their investigations of the use pulsed electromagnetic induction in determining the depths of small metallic objects (e.g., unexploded ordnance) buried up to 2 m below the surface. Depth was found by relating the ratio of time-domain electromagnetic signals in two coils. The authors noted that the strength of the response produced by an object depends upon its electrical properties, its size and shape, and its position and orientation with respect to the coils. To study these dependence Das et al modelled spherical and prolate spheroidal metallic objects in terms of electric and magnetic dipoles, and applied the principle of reciprocity to obtain the induced electromagnetic field in the coils. Limitations of simple detection and location strategies were identified.

5. SUMMARY AND CONCLUDING REMARKS

In this draft report we discussed sensor technology, data fusion and data interpretation approaches of possible maximal usefulness for subsurface imaging and characterization of land-fill waste sites. Two sensor technologies, terrain conductivity using electromagnetic induction and ground penetrating radar, were described and the literature on the subject was reviewed.

We identified the maximum entropy stochastic method as one providing a rigorously justifiable framework for fusing the sensor data. We included a brief summary of work done by us in this area in our discussion of work done in geophysics and other disciplines where inversion problems are encountered.

We conclude by mentioning some specific applications of the maximum entropy method to site characterization. These are:

1. Recalibration of instrument parameters by simultaneously varying data features and instrument parameters.

2. Removal of noise, artifacts and anomalies. In both terrain conductivity and ground penetrating radar data, systematic errors are present in a variety of forms ranging from specularities and distortions to side lobe and boundary effects.

3. Use of generalized entropy and Bayesian priors to incorporate target signatures into automated data interpretation modules.

4. MaxEnt mapping for optimally combining terrain conductivity and ground penetrating radar data, and matching features in the two sensor domains.

REFERENCES

1. Arulanandan, K.,"Dielectric Method for Prediction of Porosity of Saturated Soil," J. Geotechnical Eng., Vol. 117, pp. 319-327 (1991).

2. Beckerman, M., "A Bayes-Maximum Entropy Method for Multi-Sensor Data Fusion," ORNL Center for Engineering Systems Advanced Research Report No. CESAR-91/34 (1991).

3. Burg, J. P., "The Relationship Between Maximum Entropy Spectra and Maximum Likelihood Spectra," Geophysics, Vol. 37, pp. 375-376 (1972).

4. Collins, M. E., "Applications of Ground-Penetrating Radar," unpublished report (1991).

5. Collins, M. E., W. E. Puckett, G. W. Schellentrager and N. A. Yust, "Using GPR for Micro-Analysis of Soils and Karst Features on the Chiefland Limestone Plain in Florida," Geoderma, Vol. 47, pp. 159-170 (1990).

6. Dalan, R. A., "Defining Archaeological Features with Electromagnetic Surveys at the Cahokia Mounds State Historic Site," Geophysics, Vol. 56, pp. 1280-1287 (1991).

7. Das, Y., J. E. McFee and R. H. Chesney, "Determination of the Depth of Shallowly Buried Objects by Electromagnetic Induction," IEEE Trans. on Geoscience and Remote Sensing, Vol. GE-23, pp. 60-66 (1985).

8. Das, Y., J. E. McFee, J. Toews and G. C. Stuart, "Analysis of an Electromagnetic Induction Detector for Real-Time Location of Buried Objects," IEEE Trans. on Geoscience and Remote Sensing, Vol. 28, pp. 278-288 (1990).

9. Frohlich, B. and W. J. Lancaster, "Electromagnetic Surveying in Current Middle Eastern Archaeology: Application and Evaluation," Geophysics, Vol. 51, pp. 1414-1425 (1986).

10. Gull, S. F. and G. J. Daniell, "Image reconstruction from Incomplete and Noisy Data," Nature, Vol. 272, pp. 686-690 (1978).

11. Gull, S. F. and J. Skilling, "Maximum Entropy Method in Image Processing," IEE Proceedings, Vol. 131, Pt. F, pp. 646-659 (1984).

12. Hill, D. A, "Near-Field Detection of Buried Dielectric Objects," IEEE Trans. on Geoscience and Remote Sensing, Vol. 27, pp. 364-368 (1989).

13. Horton, K. A., R. M. Morey, R. H. Beers, V. Jordan, S. S. Sandler and L. Isaacson, "An Evaluation of Ground Penetrating Radar for Assessment of Low Level Nuclear Waste Disposal Sites," NUREG/CR-2212 (1982).

14. Jacobs, F. J. and P. A. G. van der Geest, "Spiking Band-Limited Traces with a Relative Entropy Algorithm," Geophysics, Vol. 56, pp. 1003-1014, (1991).

15. Lacoss, R. T., "Data Adaptive Spectral Analysis Methods," Geophysics, Vol. 36, pp. 661-675 (1971).

16. McNeill, J. D., Geonics Ltd. Technical Notes Nos. TN-5 and TN-6 (1980).

17. Michiguchi, Y, K. Hiramoto, M. Nishi, F. Takahashi, T. Ohtaka and M. Okada, "Development of Signal Processing Methods for Imaging Buried Pipes," IEEE Trans. on Geoscience and Remote Sensing, Vol. GE-25, pp. 11-15 (1987).

18. Michiguchi, Y., K. Hiramoto, M. Nishi, T. Ootaka and M. Okada, "Advanced Subsurface Radar System for Imaging Buried Pipes," IEEE Trans. on Geoscience and Remote Sensing," Vol. 26, pp. 733-740 (1988).

19. Nyquist, J. E. and M. S. Blair, "A Geophysical Tracking and Data Logging System: Description and Case History," Geophysics, Vol. 56, pp. 1114-1121 (1991).

20. Oldenburg, D. W., "Calculation of Fourier Transforms by the Backus-Gilbert Method," Geophys. J. R. astr. Soc., Vol. 44, pp. 413-431 (1976).

21. Schneider, J., J. Brew and I. C. Peden, "Electromagnetic Detection of Buried Dielectric Objects," IEEE Trans. on Geoscience and Remote Sensing, Vol. 29, pp. 555-562 (1991).

22. Shore, J. E., "Minimum Cross-Entropy Spectral Analysis," IEEE Trans. on Acoustics, Speech and Signal Processing, Vol. ASSP-29, pp. 230-237 (1981).

23. Sibisi, S., "Two-Dimensional Reconstructions from One Dimensional Data by Maximum Entropy," Nature, Vol. 301, pp. 134-136 (1983).

24. Smith, G. S. and W. R. Scott, "A Scale Model for Studying Ground Penetrating Radars," IEEE Trans. on Geoscience and Remote Sensing, Vol. 27, pp. 358-363 (1989).

25. Wobschall, D. "A Theory of the Complex Dielectric Permittivity of Soils Containing Water: The Semidispersive Model," IEEE Trans. on Geoscience Electronics, Vol. GE-15, pp. 49-58 (1977).

Table 1.

Cation electrical conductivities for selected clays[1]

Clay type	CEC (me/100g)
kaolinite	3-15
illite	10-40
montmorillonite	80-150

[1] From McNeill [16] (after Keller and Frischknecht, Electrical Methods in Geophysical Prospecting (New York: Pergamon Press, 1966)).

Table 2.

Conductivities and dielectric constants for selected materials[1]

Material	Electrical Conductivity (dS/m)	Dielectric Constant
air	0	1
fresh water	10^{-3} to 10^{-1}	81
sea water	40 to 50	81-88
sand[2]	10^{-3} to 10^{-1}	30
silt[2]	10^{-2} to 10^{-1}	10
clay[2]	1 to 10	8-12

[1] From Collins [4] (after Johnson, et. al, Soil Crop Sci. Soc. Fla. Proc., Vol. 30, pp. 68-72 (1979)).

[2] Fresh water saturated.

FIGURES

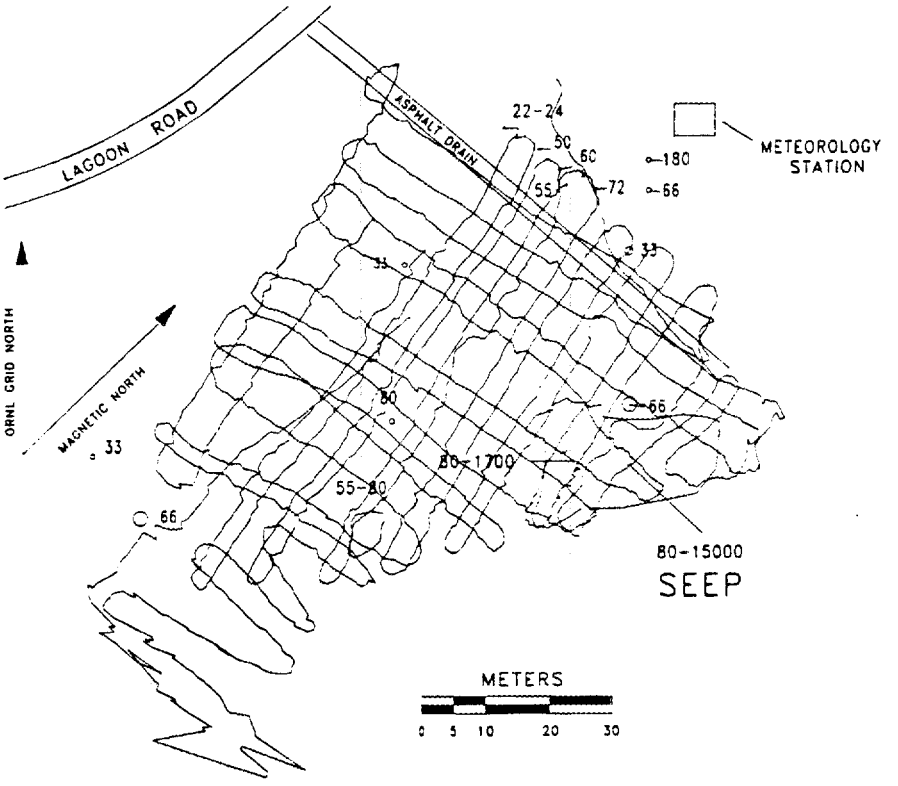

Fig.1. Map showing the section of Solid waste Storage Area 4 SWSA4 covered by the terrain conductivity survey. The stippled area had anomalous gamma radiation levels measured in microrads per hour (from Nyquist and Blair [19]).

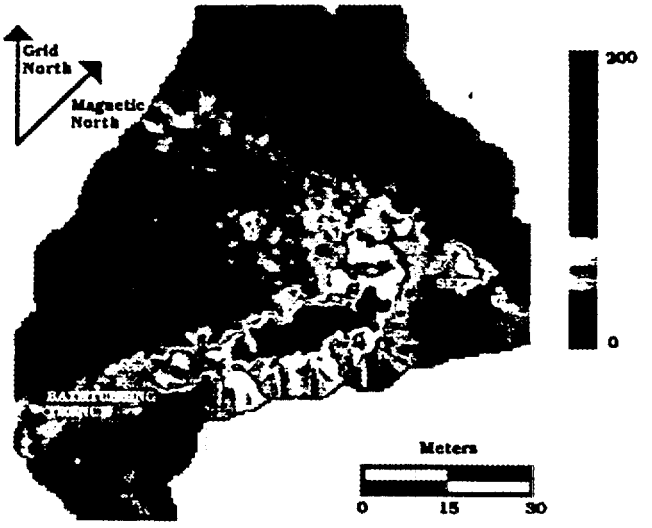

Fig. 2. Quadrature data showing the apparent conductivity (from Nyquist and Blair [19]).

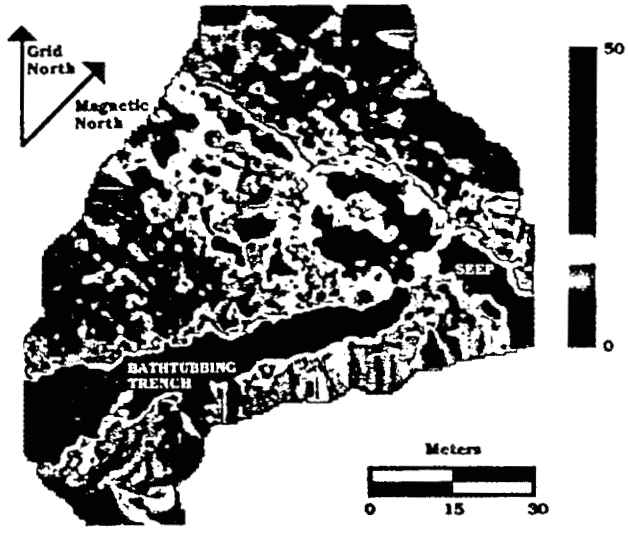

Fig. 3. In-phase data showing the apparent conductivity (from Nyquist and Blair [19]).

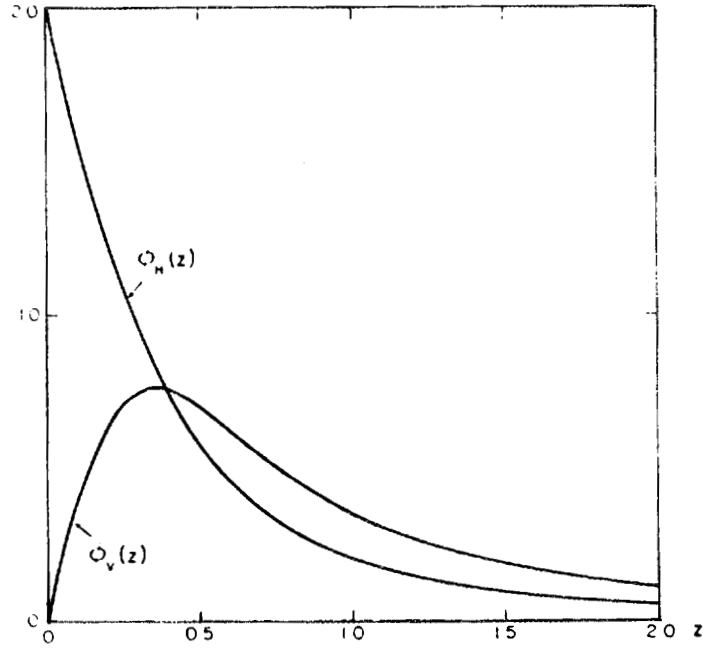

Fig. 4. Comparison of relative responses for vertical and horizontal dipoles (from McNeill [16]).

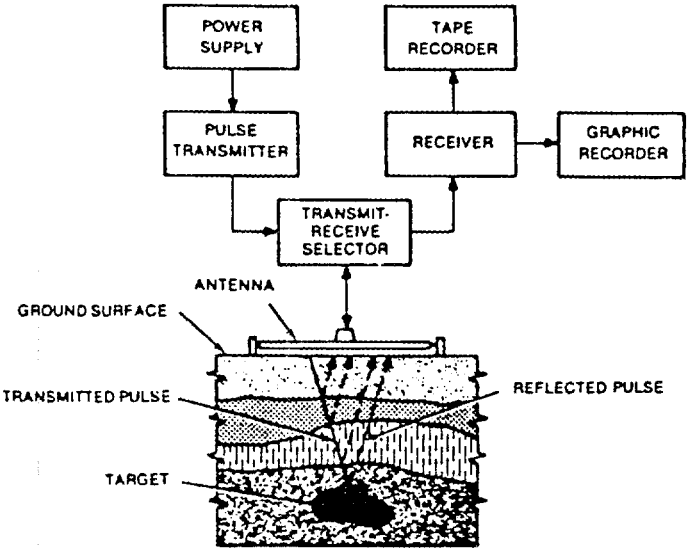

Fig. 5. Block diagram of a ground penetrating radar system (from Horton, et al [13]).

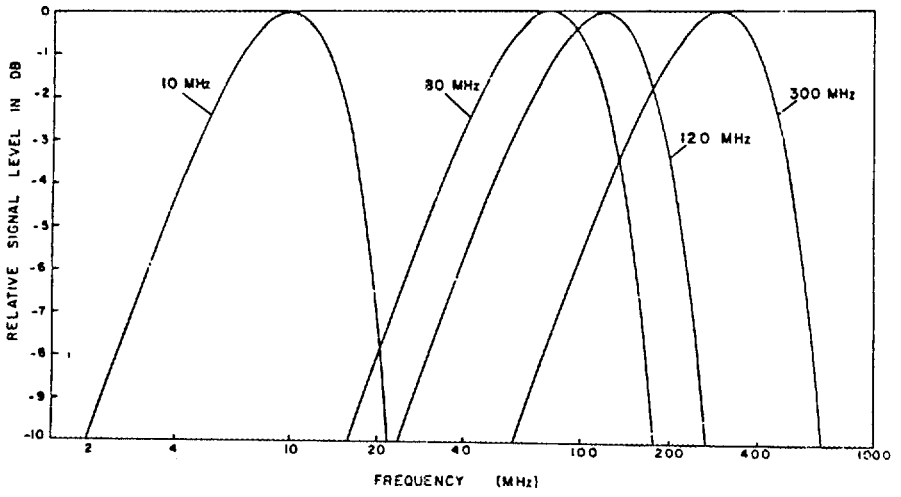

Fig. 6. Frequency spectra for different central frequencies (from Horton, et al [13]).

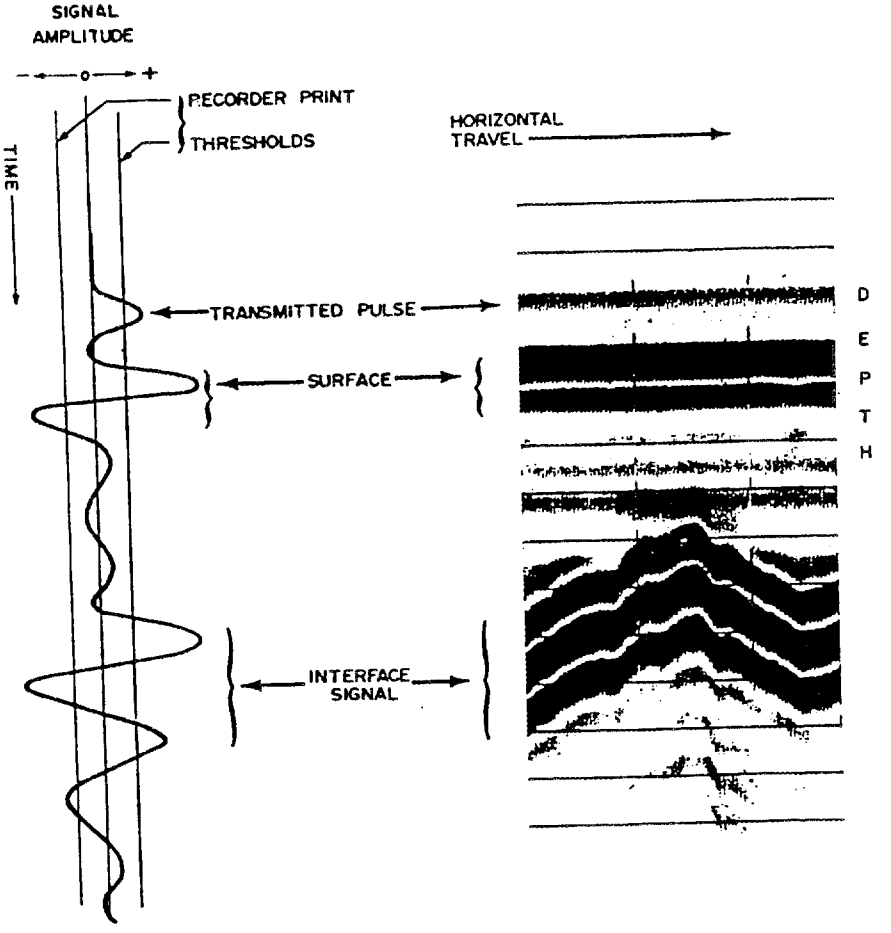

Fig. 7. Schematic diagram of a typical waveform, and an example of the corresponding data on a graphic recorder (from Horton, et al [13]).

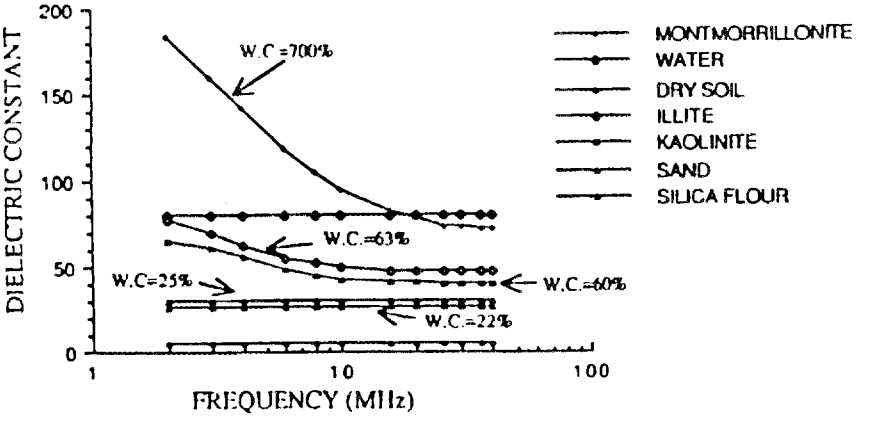

Fig. 8. Variation of the dielectric constant as a function of frequency for various materials (from Arulanandan [1]).

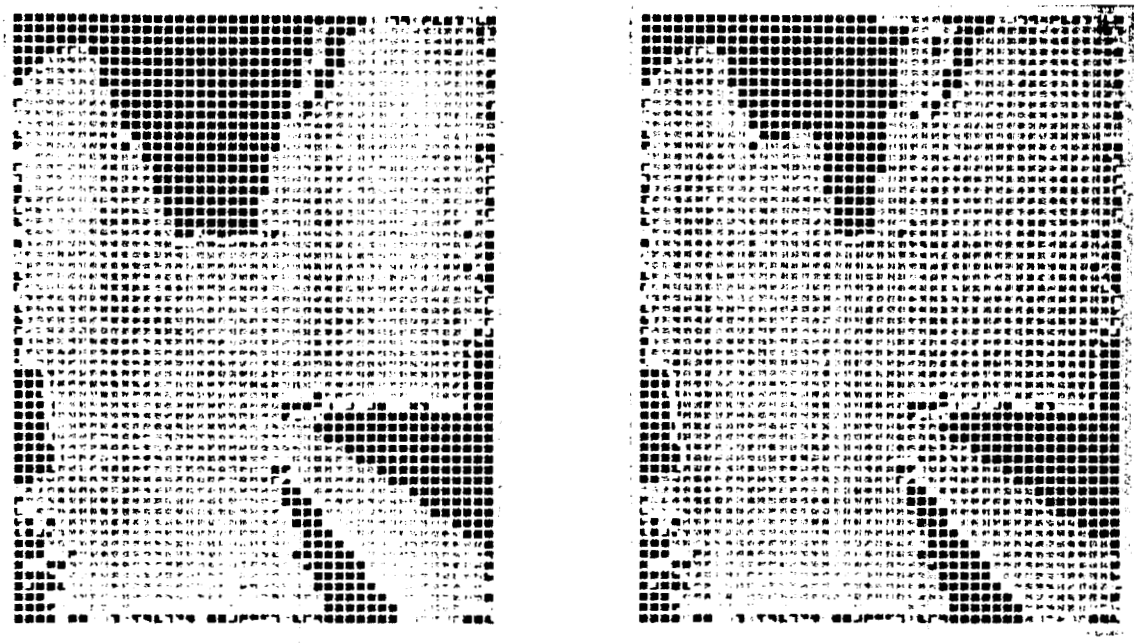

Fig. 9. Max Ent maps of the robot's environment showing empty (grey), unknown (black) and occupied (white) regions of space (from Beckerman [2]).

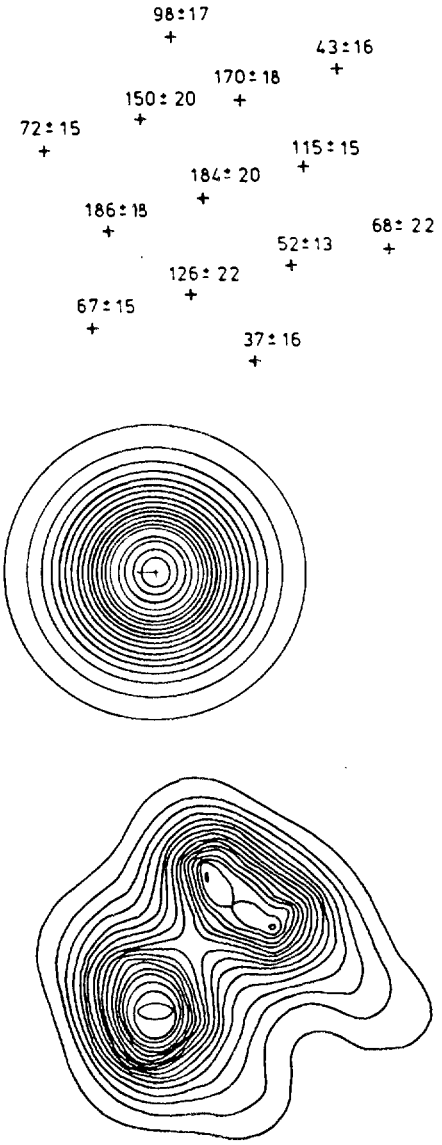

Fig. 10. Max Ent maps for various positions near Cassiopeia A (from Gull and Daniell [10]).

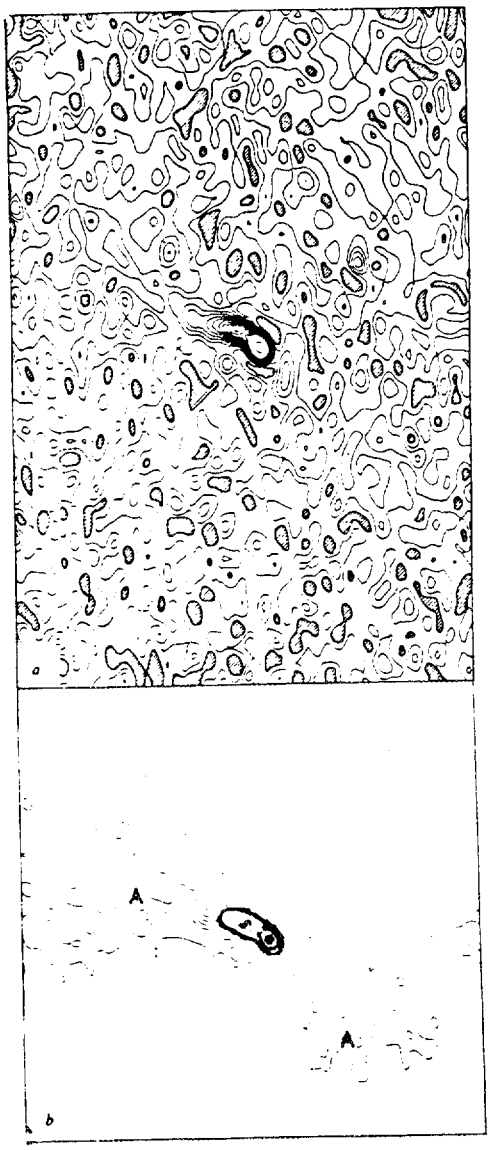

Fig. 11. Comparison of conventional (upper) and MaxEnt maps of the radio source 3C66. Cross-hatched regions are negative. Region of low contrast are indicated by the letter "A" (from Gull and Daniell [10]).

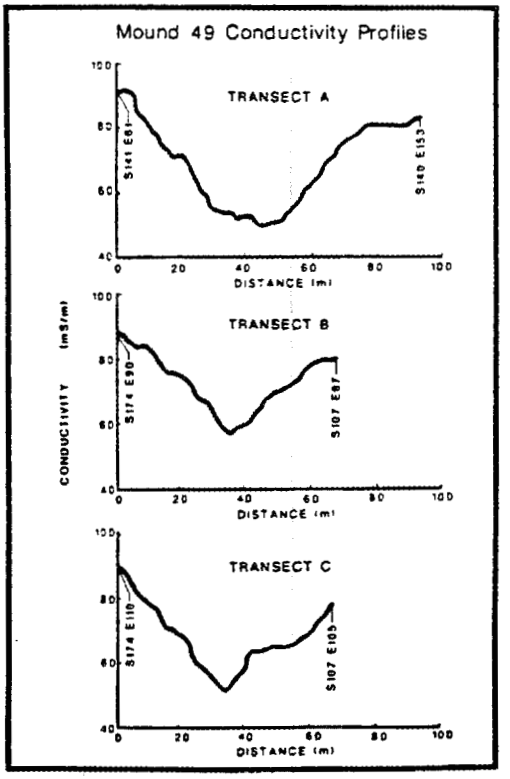

Fig. 12. EM31 transect across a well-defined mound (from Dalan [6]).

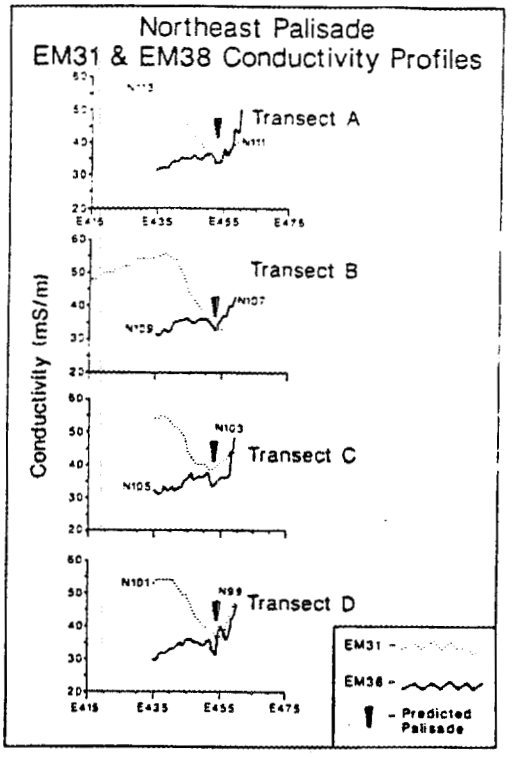

Fig. 13. EM31 and EM38 profiles, northeast palisade survey (from Dalan [6]).

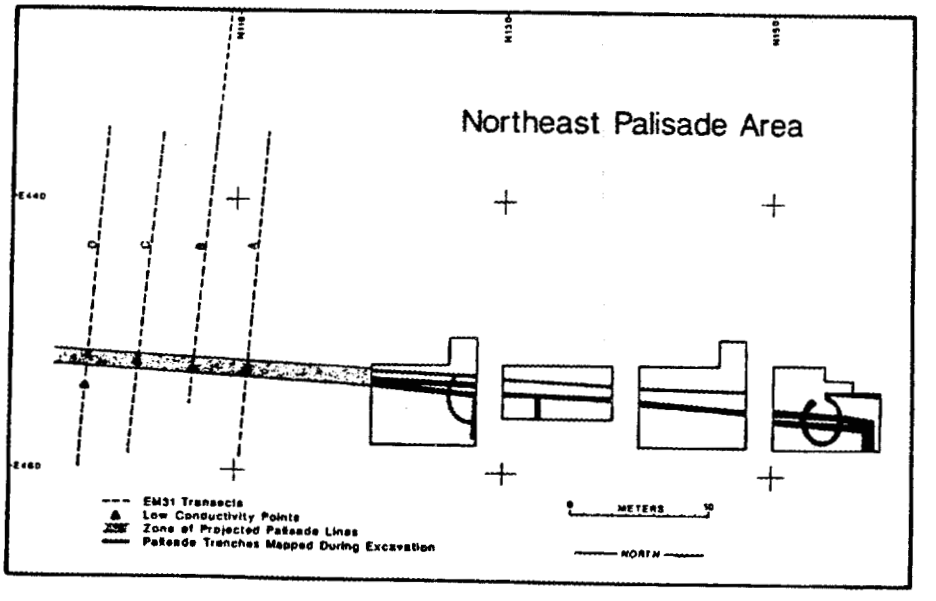

Fig. 14. Comparison of EM31 survey results and excavation data, northeast palisade survey (from Dalan [6]).

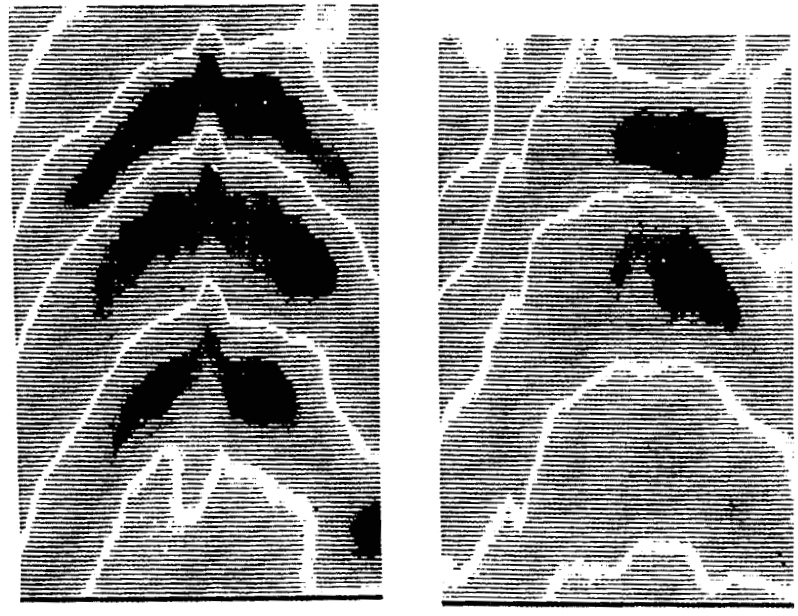

Fig. 15. Enlargement of radar profiles of a buried drum oriented vertically (left panel) and horizontally (right panel) (from Horton et al [13]).

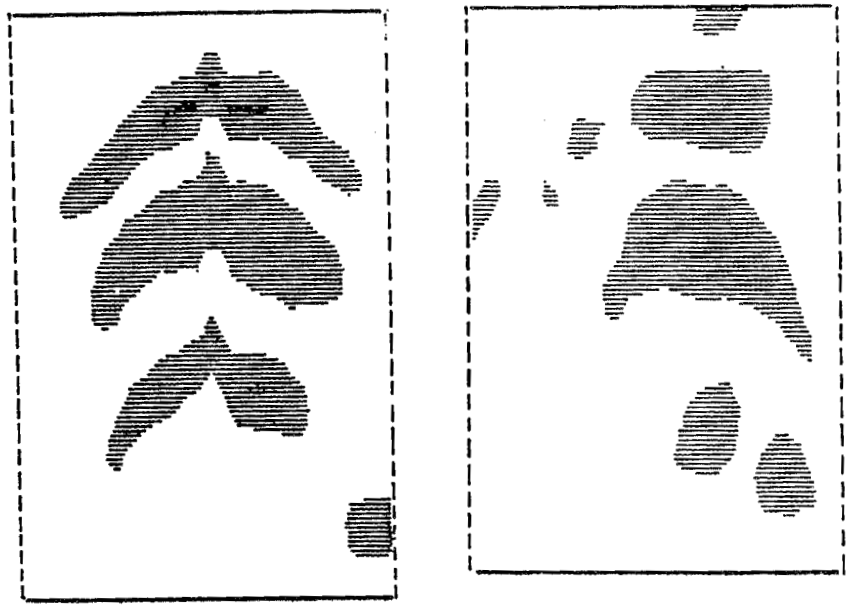

Fig. 16. Crescent images corresponding to Fig. 15 after thresholding (from Horton et al [13]).

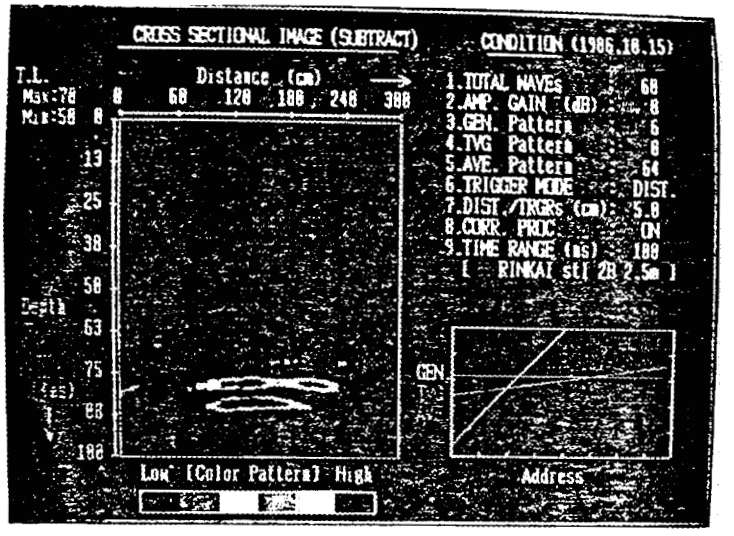

Fig. 17. Typical imaging results for buried pipes (from Michiguchi et al [18]).

Left Blank Intentionally

ORNL/TM-11971
CESAR-91/39

INTERNAL DISTRIBUTION

1. B. R. Appleton
2. S. M. Babcock
3. J. E. Baker
4. A. L. Bangs
5- 9. M. Beckerman
10. B. L. Burks
11. J. R. Einstein
12. C. W. Glover
13. W. R. Hamel
14. J. N. Herndon
15. J. P. Jones
16. H. E. Knee
17. R. L. Kress
18. G. E. Liepins
19-23. R. C. Mann
24. S. A. Meacham
25. E. M. Oblow
26. F. G. Pin
27. D. B. Reister
28. B. S. Richardson
29. P. F. Spelt
30-34. F. J. Sweeney
35. M. A. Unseren
36-40. R. C. Ward
41. R. W. Brockett (Consultant)
42. J. J. Dorning (Consultant)
43. J. E. Leiss (Consultant)
44. N. Moray (Consultant)
45. M. F. Wheeler (Consultant)
46. EPMD Reports Office
47. Central Research Library
48. Document Ref. Section
49-50. Laboratory Records
51. Laboratory Records-RC
52. ORNL Patent Office

EXTERNAL DISTRIBUTION

53. Office of Assistant Manager, Energy Research and Development, DOE Field Office, Oak Ridge, P. O. Box 2008, Oak Ridge, TN. 37831
54. Dr. Peter Allen, Department of Computer, Columbia University, 450 Computer Science, New York, NY. 10027
55. Dr. Wayne Book, Department of Mechanical Engineering, Georgia Institute of Technology, J. S. Coon Building, Room 306, Atlanta, GA. 30332
56. Dr. Steven Dubowsky, Building 3, Room 469A, Massachusetts Institute of Technology, Cambridge, MA. 02139
57. Dr. Avi Kak, Department of Electrical Engineering, Purdue University, Engineering Mall, LaFayette, IN. 47907

58. Dr. Wes Snyder, Department of Radiology, Bowman Gray School of Medicine, 300 S. Hawthorne Drive, Winston Salem, NC. 27103
59. O. P. Manley, Division of Engineering and Geosciences, Office of Basic Energy Sciences, U. S. Department of Energy, Washington, DC. 20585
60. H. Alter, Office of Technology Support Programs, U. S. Department of Energy, Washington, DC. 20585
61-70. Office of Scientific and Technical Information, P. O. Box 62, Oak Ridge, TN. 37831